TABLE OF CONTENTS

LIST OF FIGURES

LIST OF TABLES

CHAPTER 1

Introduction

CHAPTER 2

Dihadron correlation measurements as a method to study saturation

2.1 Dihadron Correlations in the Saturation Formalism

According to the effective small-x k_t factorization established in Ref. [DMX11], which is briefly summarized above, the back-to-back correlation limit of the dihadron production cross section can be used to directly probe the WW gluon distribution $xG^{(1)}(x, q_\perp)$. As a comparison, the hadron production in semi-inclusive deep inelastic scattering (SIDIS), as shown in Ref. [MXY09], is related to the so-called dipole gluon distributions $xG^{(2)}(x, q_\perp)$.

The coincidence probability $C(\Delta\phi) = \frac{N_{pair}(\Delta\phi)}{N_{trig}}$ is a commonly exploited observable in dihadron correlation studies, in which $N_{pair}(\Delta\phi)$ is the yield of the correlated trigger and associate particle pairs, while N_{trig} is the trigger particle yield. This correlation function $C(\Delta\phi)$ depends on the azimuthal angle difference $\Delta\phi$ between the trigger and associate particles. In terms of theoretical calculation, the correlation function is defined as

$$C(\Delta\phi) = \frac{1}{\frac{d\sigma_{\text{SIDIS}}^{\gamma^*+A \to h_1+X}}{dz_{h1}}} \frac{d\sigma_{\text{tot}}^{\gamma^*+A \to h_1+h_2+X}}{dz_{h1}dz_{h2}d\Delta\phi}. \tag{2.1}$$

Let us consider a process of a virtual photon scattering on a dense nuclear target producing two final state back-to-back $q\bar{q}$ jets: $\gamma^* + A \to q(k_1) + \bar{q}(k_2) + X$, in which k_1 and k_2 are the four momenta of the two outgoing quarks. This process is the dominant one in the low-x region, since the gluon distribution is much larger than the quark distributions

inside a hadron at high energy. The back-to-back correlation limit indicates that the transverse momentum imbalance is much smaller than each individual momentum: $q_\perp = |k_{1\perp} + k_{2\perp}| \ll P_\perp$, with $P_\perp$ defined as $(k_{1\perp} - k_{2\perp})/2$. At leading order (LO), the dihadron total cross section, which includes both the longitudinal and transverse contributions, can be written as follows [DMX11]:

$$
\frac{d\sigma_{\text{tot}}^{\gamma^*+A\to h_1+h_2+X}}{dz_{h1}dz_{h2}d^2p_{h1\perp}d^2p_{h2\perp}} = C\int_{z_{h1}}^{1-z_{h2}} dz_q \frac{z_q(1-z_q)}{z_{h2}^2 z_{h1}^2} d^2p_{1\perp}d^2p_{2\perp}\mathcal{F}(x_g,q_\perp)\mathcal{H}_{\text{tot}}(z_q,k_{1\perp},k_{2\perp}) \quad (2.2)
$$
$$
\times \sum_q e_q^2 D_q\left(\frac{z_{h1}}{z_q},p_{1\perp}\right)D_{\bar{q}}\left(\frac{z_{h2}}{1-z_q},p_{2\perp}\right),
$$

where $C = \frac{S_\perp N_c \alpha_{em}}{2\pi^2}$ gives the normalization factor, with $S_\perp$ being the transverse area of the target, z_q is the longitudinal momentum fraction of the produced quark with respect to the incoming virtual photon, $\mathcal{H}_{\text{tot}}$ is the combined hard factor, $k_{1\perp}$ and $k_{2\perp}$ are the transverse momenta of the two quarks, while $p_{h1\perp}$ and $p_{h2\perp}$ are the transverse momenta of the two corresponding produced hadrons respectively. $\mathcal{F}(x_g, q_\perp)$ comes from the relevant WW gluon distribution $xG^{(1)}(x_g, q_\perp)$ evaluated with the gauge links for a large nucleus at small x by using the McLerran-Venugopalan model [MV94],

$$
\mathcal{F}(x_g,q_\perp) = \frac{1}{2\pi^2}\int d^2r_\perp e^{-iq_\perp r_\perp}\frac{1}{r_\perp^2}[1-\exp(-\frac{1}{4}r_\perp^2 Q_s^2)], \quad (2.3)
$$

in which $x_g = \frac{z_q p_{h1\perp}^2}{z_{h1}^2 s} + \frac{(1-z_q)p_{h2\perp}^2}{z_{h2}^2 s} + \frac{Q^2}{s}$ is the longitudinal momentum fraction of the small-x gluon with respect to the target hadron and Q_s is the gluon saturation scale. $D_q\left(\frac{z_h}{z_q}, p_\perp\right)$ represents the transverse momentum dependent fragmentation functions, where $p_\perp$ shows the additional transverse momentum introduced by fragmentation processes.

In principle, the so-called linearly polarised gluon distribution [MZ11, DQX12] also contributes to the dihadron correlation and can be systematically taken into account. This part of the contribution comes from an averaged quantum interference between a scattering amplitude and a complex conjugate amplitude with active gluons linearly polarized in two orthogonal directions in the azimuthal plane. Numerical calculation shows that this contribution is negligible for dihadron back-to-back correlations. Also, this type of contribution vanishes when the dihadron correlation function is averaged over the azimuthal angle of the trigger particle.

As to the single-inclusive-hadron production cross section, which enters the denominator of the definition of the correlation function $C(\Delta\phi)$, it can be calculated from the saturation physics/CGC formalism [MXY09] as follows:

$$\frac{d\sigma^{\gamma^*+A\to h_1+X}_{\text{SIDIS}}}{dz_{h1}d^2p_{h1\perp}} = C\int_{z_{h1}}^1 dz_q \int d^2q_\perp F_{x_g}(q_\perp)H_{\text{SIDIS}}(k_\perp,q_\perp,Q) \tag{2.4}$$
$$\times \sum_q e_q^2 \frac{z_q}{z_{h1}^2}D_q\left(\frac{z_{h1}}{z_q}\right),$$

where H_{SIDIS} is the $q_\perp$ dependent hard factor for SIDIS, which includes both the longitudinal and transverse photon contribution. Here $F_{x_g}(q_\perp)$, which is related to $xG^2(x_g,q_\perp)$, is the Fourier transform of the dipole cross section:

$$F_{x_g}(q_\perp) = \int \frac{d^2r}{2\pi^2}e^{iq_\perp\cdot r_\perp}\frac{1}{N_c}Tr\langle U(r_\perp)U^\dagger(0)\rangle_\rho \tag{2.5}$$
$$\simeq \frac{1}{\pi Q_{sA}^2}\exp\left[-\frac{q_\perp^2}{Q_{sA}^2}\right].$$

It has been suggested in Refs [DMM11, DJL11] that both dipole and WW gluon distributions have similar geometric scaling behavior. Therefore, one can parameterize these gluon distributions following the Golec-Biernat Wüsthoff (GBW) [GW98] model calculation, in which $Q_{sA}^2(x) = c(b)A^{1/3}Q_{s0}^2(x/x_0)^{-\lambda}$, with $Q_{s0} = 1$ GeV, $x_0 = 3.04\times 10^{-4}$ and $\lambda = 0.288$. The gluon saturation momentum is related to $Q_{sA}^2(x)$ by $Q_s^2(x) = \frac{2N_c^2}{N_c^2-1}Q_{sA}^2(x)$. $c(b) = c(0)\sqrt{1-b^2/R^2}$ gives the nuclear profile dependence with a radius R, where b is the impact parameter. As it is not an easy task to determine the exact impact parameter in e+A collisions, a median number $c(b) = 0.8$ is used for the estimation, which is supposed to average the nucleus geometry effectively. The parametrized DSS fragmentation function [FSS07], $D(z,p_\perp) = D(z)\frac{1}{\pi\langle p_\perp^2\rangle}e^{\frac{-p_\perp^2}{\langle p_\perp^2\rangle}}$ with $\langle p_\perp^2\rangle = 0.2\,\text{GeV}^2$, is used to compute the hadron production.

By utilizing Eq. (2.2) and Eq. (2.4), one can straightforwardly calculate the coincidence probability. The theoretical prediction at the Born level for the suppression of the away-side of the dihadron correlation measurement is shown by the solid curves in Fig. 2.1.

All the above results are estimated based on the LO Born level contribution. At the EIC energy scale the one-loop contribution [MXY13b], which is also known as the

so-called Sudakov factor, can be important as well. To include the Sudakov factor contribution at leading double logarithm level, one can rewrite the relevant WW distribution as follows [MXY13a]:

$$\mathcal{F}(x_g, q_\perp) = \frac{1}{2\pi^2} \int d^2 r_\perp e^{-iq_\perp r_\perp} \frac{1}{r_\perp^2} [1 - \exp(-\frac{1}{4} r_\perp^2 Q_s^2)] \exp[-\frac{\alpha_s N_c}{4\pi} \ln^2 \frac{K^2 r_\perp^2}{c_0^2}], \qquad (2.6)$$

where K^2 represents the hard momentum scale in two-particle production processes. It can be chosen as $K^2 = P_\perp^2$ or $K^2 = Q^2$, depending on which one is larger, and $c_0 = 2e^{-\gamma_E}$ with the Euler constant γ_E. It is known that the single logarithmic terms as well as the next-to-leading order (NLO) contribution of the Sudakov factor also have sizeable contributions compared to the above leading double logarithmic contribution. Therefore, the numerical value of α_s in the Sudakov factor used in this calculation may be different from what one normally expects according to a QCD running coupling constant calculation.

One needs to pay attention to the applicability of this calculation. As the GBW model is not sufficient to describe the UGDs in the region where $q_\perp$ is much larger than Q_s, we should limit this calculation to the saturation region ($x_g < 0.01$) to ensure the GBW model can be applied. Additionally, to ensure that the power corrections to the two-particle production are negligible, one needs the magnitude of the jet transverse momenta $P_\perp$ to be much larger than Q_s.

The current calculations are performed for Q^2 of the same order as $P_\perp^2$. For pair production, the Sudakov factor is usually due to a scale difference between $P_\perp$ and the dijet momentum imbalance $q_\perp$. Because we have required that $P_\perp \gg q_\perp$ as discussed above, it is necessary to include the Sudakov contribution. As for the trigger hadron inclusive cross section, the Sudakov factor is not important, since the trigger hadron p_T is of the same order as Q and $P_\perp$. An illustration of this Sudakov effect with $\alpha_s = 0.35$ can be found in Fig. 2.1 labeled by the dashed lines. It is worthwhile to point out that the Sudakov effect in a nuclear environment is still not very well known. In the current small x scenario as shown in Eq. (2.6), it is convoluted with the gluon distribution function. The theoretical calculation indicates that the Sudakov factor has no nuclear A dependence at LO. As shown in Fig. 2.1, the away-side suppression of the dihadron
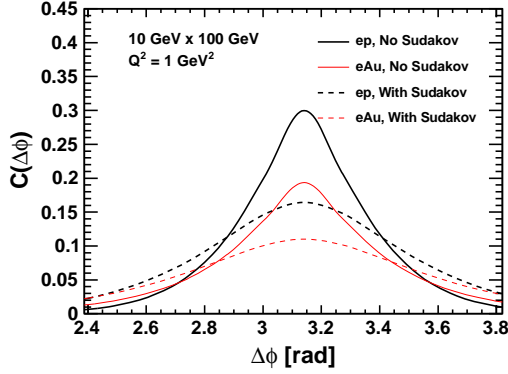
Figure 2.1: [color online] π^0-correlation curves calculated in the saturation formalism at 10 GeV×100 GeV for $e + p$ (thick line) and e+Au (thin line) with (dashed curve) and without (solid curve) the Sudakov factor. The kinematics chosen are $y = 0.7$, $Q^2 = 1\,\mathrm{GeV}^2$, $z_{h1} = z_{h2} = 0.3$, $p_{h1\perp} > 2\,\mathrm{GeV}/c, 1\,\mathrm{GeV}/c < p_{h2\perp} < p_{h1\perp}$.

correlation is due to the combination of the Sudakov suppression and saturation effects. It is conceivable that the suppression due to saturation effects shall become more and more dominant when the ion beam species are changed from proton to gold, while the Sudakov effect remains more or less the same.

2.2 Electron-Ion Collider and Simulations

2.2.1 The Electron-Ion Collider and its Detector

Two independent designs for an EIC are being developed in the United States: eRHIC, at Brookhaven National Laboratory (BNL); and MEIC/ELIC at Thomas Jefferson National Laboratory (JLab). The following studies will focus on the eRHIC version of an EIC and the new model detector at eRHIC. The eRHIC design at BNL reuses the available infrastructure and facilities of RHIC's high-energy polarized proton/ion beam. A new electron beam, based on Energy Recovery LINAC (ERL) technology, is to be built inside the current RHIC tunnel. At eRHIC, the collision luminosity is expected to be in the order of $10^{33-34}\mathrm{cm}^{-2}\mathrm{s}^{-1}$. The full range of proton/ion beam energies will be accessible from the beginning of operations, while the electron beam energy will start with $10-15$
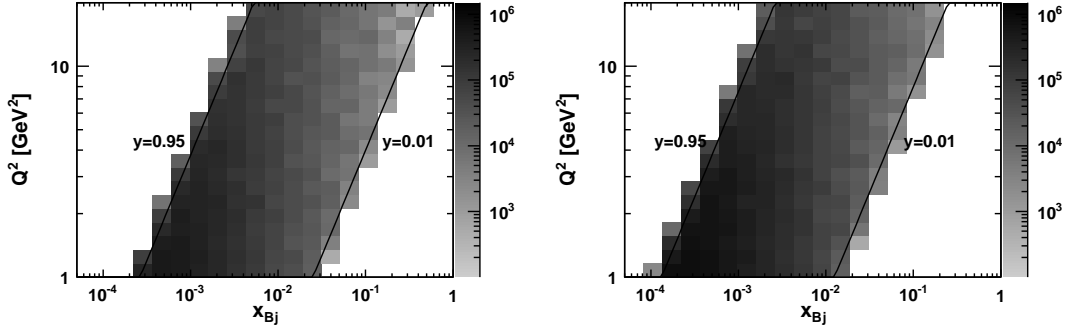
Figure 2.2: Expected yields of charged particle pairs at transverse momentum $p_T > 1\,\text{GeV}/c$ in bins of (Q^2, x_{Bj}) for an integrated luminosity of $1\,fb^{-1}$ for $e + p$ 10 GeV $\times$100 GeV (Left) and 20 GeV $\times$100 GeV (Right) in the kinematic range of $1\,\text{GeV}^2 < Q^2 < 20\,\text{GeV}^2$, and $0.01 < y < 0.95$.

GeV and later be increased to 20 GeV.

The tracking system of the baseline eRHIC detector will consist of a TPC, GEM and silicon detectors spanning a range of $-4 < \eta < 4$ in pseudorapidity. The end-cap and barrel region on the detector will be equipped with electromagnetic calorimeters covering $-4.5 < \eta < 4.5$. Hadronic calorimeter will be used mostly for jet physics at full energy in the forward (hadron beam going direction) and backward (electron beam going direction) rapidities spanning $2 < |\eta| < 4.5$. Projected momentum and energy resolutions of these devices are better than a few percent, which extends the capability of this detector to a large variety of physics topics.

The present study is based on the planned lepton and nucleon beam energy of 10 GeV $\times$ 100 GeV and 20 GeV $\times$ 100 GeV. The kinematics are constrained to the main region of interest for dihadron correlation studies, $1\,\text{GeV}^2 < Q^2 < 20\,\text{GeV}^2$ and $0.01 < y < 0.95$. Backward electromagnetic calorimetry and the TPC are utilized for reconstruction of the event kinematics (based on the scattered electron). As shown in Fig. 2.2, abundant high-p_T particles will be generated in the specified kinematic region to make correlated hadron pairs even with a limited luminosity of $1\ fb^{-1}$. Among those generated high-p_T particles, Fig. 2.3 suggests that gluon dijet processes dominate in the production of particles with a transverse momentum greater than 2 GeV/c and charged pions are the major component for the final state particles.
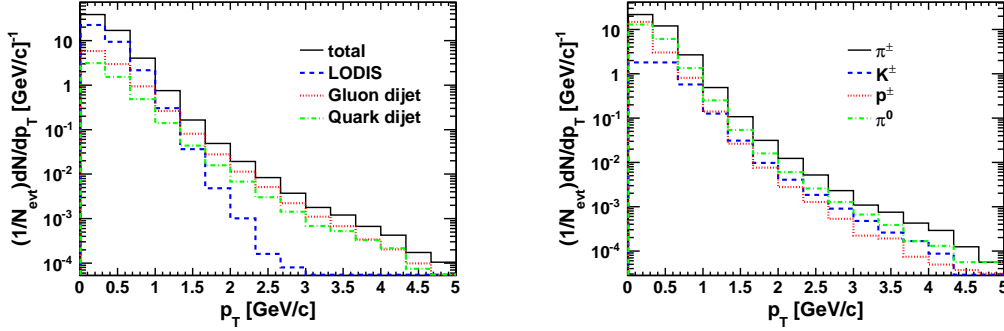
Figure 2.3: [color online] Particle p_T distributions for $e + p$ 10 GeV × 100 GeV collisions with $1\,\text{GeV}^2 < Q^2 < 20\,\text{GeV}^2, 0.01 < y < 0.95$. Left: charged particle production from LO DIS, gluon dijets (PGF and resolved gluon channel) and quark dijets (QCDC and resolved quark channel). Right: $\pi^{\pm}, K^{\pm}, p^{\pm}$ and π^0 production for all processes.

2.2.2 Monte Carlo Set Up

The simulation part of this study is based on the PYTHIA-6.4 Monte Carlo program, with the PDF input from the LHAPDF library [WBG05] and JETSET used for fragmentation processes. If one defines $\hat{p_T}$ as the transverse momentum of final state partons in the center of mass system of the hard interaction, the factorization scale μ^2 of $2 \to 2$ processes can be expressed as $\mu^2 = \hat{p_T}^2 + \frac{1}{2}Q^2$.

In PYTHIA, depending on the wave function components for the incoming virtual photon, various subprocesses are divided into three major classes: the direct processes, the VMD processes and the anomalous processes [FS00], as illustrated in Fig. 2.4. The direct photon interacts as a point-like particle with the partons of the nucleon, while the VMD and anomalous components interact through their hadronic structure. The VMD component is characterized by non-perturbative fluctuations of the photon into a $q\bar{q}$ pair existing long enough to evolve into a hadronic state before the subsequent interaction with the nucleon [BSY78]. This process can be described in the VMD model, where the hadronic state is treated as a vector meson (e.g. ρ^0, ω, ϕ) with the same quantum numbers as the photon. These VMD states can undergo all the soft/hard interactions with the nucleon allowed in hadronic physics. The large-scale, perturbatively fluctuated
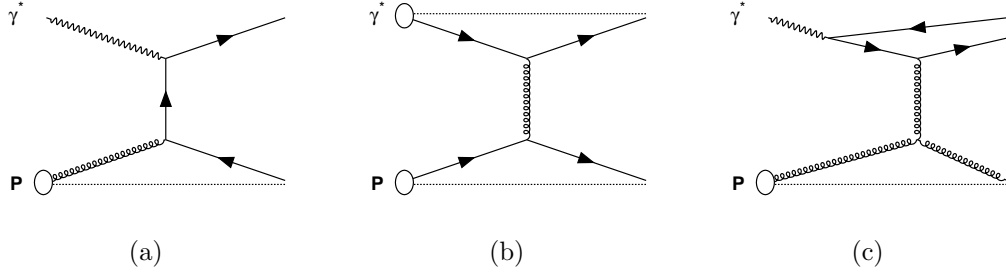
Figure 2.4: Feynman diagrams for different PYTHIA subprocesses contributing to the hard interaction: (a) direct, (b) VMD, (c) anomalous. The dotted lines indicate the presence of a spectator. Bubbles stand for a hadron or hadronic structure.

photons can be added as the anomalous photon part in a Generalized VMD (GVMD) model. Same pQCD $2 \to 2$ process can be developed over the VMD or anomalous state of the virtual photons on the target nucleon, with the difference that parameterized photon PDFs are used for anomalous photons whereas for the hard VMD components those vector meson PDFs are involved. Hard VMD and anomalous process are usually referred to as "resolved" process. Resolved photon processes play a significant part in the production of hard high-p_T processes at $Q^2 \approx 0$. The following hard subprocesses are grouped in the resolved processes category: $qq \to qq$, $q\bar{q} \to q\bar{q}$, $q\bar{q} \to gg$, $qg \to qg$, $gg \to q\bar{q}$, $gg \to gg$. In the high-Q^2 region, direct processes become dominant, Fig. 2.5 shows the major subprocesses in that category: LO DIS, Photon-Gluon Fusion (PGF) and QCD Compton (QCDC). As the PGF process is directly sensitive to the gluon distribution, it is extremely important for DIS dijet productions. The final conditional yield can be expressed as a superposition from different processes:

$$C(\Delta\phi) = \Sigma_i w_i w_i^s C(\Delta\phi)_i, \tag{2.7}$$

with w_i being the statistical weight of every subprocess i involved in the measurement and w_i^s is the suppression factor for the subprocess i from saturation. For the quark channels unaffected by saturation $w_i^s = 1$, while for the gluon channels, suppression of $C(\Delta\phi)$ at away-side is expected with $w_i^s < 1$.

To simulate $e + p$ events the CTEQ6M [PSH02] PDF in the $\overline{\text{MS}}$ scheme is used. For the e+A event sample, the NLO EPS09 parton distribution functions [EPS09] and hard
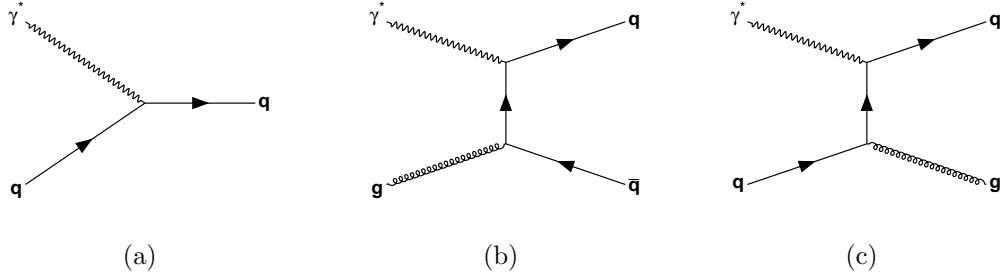
(a)　　　　　　　　　　(b)　　　　　　　　　　(c)

Figure 2.5: Feynman diagrams for the hard processes based on point-like photons: (a) $\mathcal{O}(\alpha_s^0)$ LO DIS, (b) Photon-Gluon Fusion (PGF) and (c) QCD Compton scattering (QCDC).

parton energy loss based on the medium geometry have been applied to account for nuclear effects in the simulation. Modifications of nuclear PDF have the form

$$f_i^A(x, Q^2) = R_i^A(x, Q^2) f_i^p(x, Q^2), \tag{2.8}$$

where R_i^A is the nuclear modification factor multiplied on top of the free proton PDF $f_i^p(x, Q^2)$ for a parton of flavor i, with $f_i^p(x, Q^2)$ being the CTEQ6M PDF set. Assuming isospin symmetry for protons and neutrons, the up/down quark distribution can be averaged according to the corresponding mass number A and charge number Z. The hard parton energy loss in the nuclear medium is included following the parton quenching model (PQM) formalism based on Ref [SW03]. In the energy loss picture, the medium effect is characterized by the so-called transport coefficient, defined as the average medium-induced squared transverse momentum per unit path length for a hard parton:

$$\hat{q} = \left\langle k_\perp^2 \right\rangle_{medium} / \lambda, \tag{2.9}$$

where λ is the mean free path and $k_\perp$ represents the medium-introduced transverse momentum to the hard parton. The characteristic energy loss scale is set by

$$\omega_c = \frac{1}{2} \hat{q} L^2. \tag{2.10}$$

L is the medium path length the parton traverses through. It is determined by the impact parameter at which the hard scattering occurs with respect to the geometry of the nucleus described by a Wood-Saxon distribution. Using the above parameters, one

can define the energy loss probability distribution as follows

$$P(\Delta E; R, \omega_c) = p_0(R)\delta(\Delta E) + p(\Delta E; R, \omega_c), \tag{2.11}$$

where p_0 is the probability that the parton experiences no medium induced radiation.

In the phenomenological studies of dihadron correlations, triggering on a hadron with high-p_T on average selects the most energetic hadron in events with back-to-back jets. Correlated hadron pairs reflect two important features of QCD dynamics of the hard scattering process. First, an associated hadron at the near-side allows one to probe the in-medium QCD evolution of an energetic parton, which can be viewed as the final state effect with the nuclear medium. Second, an associated hadron at the away-side, in addition to the primary hard scattering, is sensitive to the initial transverse momentum that the incoming parton carries.

For pQCD calculations in the collinear factorization framework, the PDFs and fragmentation functions do not contain any transverse momentum dependence. Therefore, the transverse momentum of hadrons produced in the final state is given by $p_T = z\hat{p_T}$, where $\hat{p_T}$ and p_T are the transverse momentum of the parton and hadron respectively. z represents the momentum fraction of a hadron with respect to its mother parton. This relation should be revised if the transverse momentum is allowed in both the PDFs and fragmentation functions.

Transverse motion of partons inside hadrons can be effectively included by assuming that the intrinsic k_T follows a Gaussian distribution. Similarly, the transverse momentum enhancement p_T^{frag} with respect to the jet direction during hadronization can also be approximated by a Gaussian distribution. The intrinsic k_T and fragmentation p_T^{frag} now both contribute to the transverse momentum of final state hadrons, which can be written as $p_T = z(k_T + \hat{p_T}) + p_T^{\mathrm{frag}}$. We follow the common practice to set the Gaussian width to 0.4 GeV for both intrinsic k_T and p_T^{frag} distributions in the simulations.

Besides all the above effects, additional soft gluon radiations, normally characterized as a parton shower can also modify the final transverse momentum, thereby impacting the dihadron correlations. In perturbative QCD calculations the parton shower are computed in terms of Sudakov form factors.
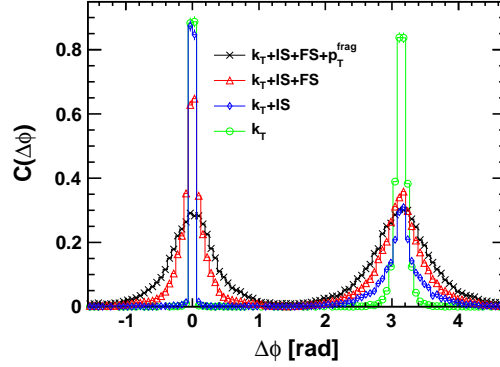
Figure 2.6: [color online] Comparison of dihadron correlation due to different physical inputs, such as intrinsic k_T, initial state parton shower (IS), final state parton shower plus resonance decay (FS) and p_T broadening in fragmentation processes. The $e + p$ data are for charged hadrons with a beam energy of 20 GeV × 100 GeV with $1.0\,\mathrm{GeV}^2 < Q^2 < 1.5\,\mathrm{GeV}^2, 0.65 < y < 0.75, p_T^{trig} > 2\,\mathrm{GeV}/c, 1\,\mathrm{GeV}/c < p_T^{assoc} < p_T^{trig}, 0.2 < z_h^{trig}, z_h^{assoc} < 0.4.$

Fig. 2.6 shows an illustration of all the possible effects available in the Monte Carlo in the simulation of the azimuthal correlation function. The open circles illustrate the dihadron correlation with only intrinsic k_T in the initial parton distribution. It is understandable that the correlation function is strongly peaked at $\Delta\phi = 0, \pi$ for this setting. Now the other effects are turned on one-by-one according to the order of their occurrences in physical processes. When the initial state (IS) parton shower is added into the simulation, as shown by the open diamonds, the away-side correlation is significantly reduced since it is very sensitive to the momentum imbalance of the dijet system, while the near-side correlation is almost unmodified. Next, we turn on the final state (FS) parton shower for the scattered parton before the fragmentation process occurs. We find that both the near-side and away-side peaks are broadened, as illustrated by the empty triangles, due to soft radiation and particle decay in the fragmentation. Lastly, we add transverse momentum dependence into the fragmentation function, labeled as p_T^{frag}, and obtain the crossings, which indicate further broadening of both peaks.

For our model of e+A implemented in PYTHIA, the effects due to energy loss in the cold nuclear medium are expected to be weak, because fast moving partons are
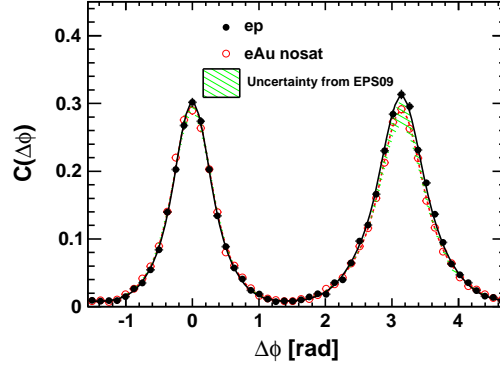
Figure 2.7: [color online] Simulated data points for particle correlations for charged hadrons in $e + p$ and e+Au collisions with beam energies of 20 GeV × 100 GeV and $1.0\,\mathrm{GeV}^2 < Q^2 < 1.5\,\mathrm{GeV}^2, 0.65 < y < 0.75, p_T^{trig} > 2\,\mathrm{GeV}/c, 1\,\mathrm{GeV}/c < p_T^{assoc} < p_T^{trig}, 0.25 < z_h^{trig}, z_h^{assoc} < 0.35$. Lines are the fit for $e + p$ or e+A points. The shaded band shows the uncertainty due to the EPS09 nuclear PDFs.

likely to fragment outside the nucleus in the considered kinematic regions. Considering that the nuclear PDF also has little impact on the p_T imbalance of dijets, it comes as no surprise to see very little change from $e + p$ to e+A in the simulation, as shown in Fig. 2.7. Table 2.1 is a reference for different effects on the relative root mean square (RMS) deviation of the near/away side azimuthal correlation function, from which we can clearly draw the conclusion that initial-state parton showers dominate the away-side peak of the correlation function, while the near-side peak is mainly controlled by final-state effects such as final-state parton showers, fragmentation p_T and possible resonance

Table 2.1: Relative Root Mean Square (RMS) for the $\Delta\phi$ distribution from $e + p$ collisions including different effects influencing the width of the near and away side peak compared to the baseline RMS with all the effects included (bottom row).

	Near-side $\Delta\phi$ RMS	Away-side $\Delta\phi$ RMS
k_T	0.21	0.25
k_T + IS	0.30	0.72
k_T + IS + FS	0.65	0.81
k_T + IS + FS + p_T^{frag}	1.00	1.00

decays in the fragmentaion.

As the saturation physics discussed above is mainly about the gluon dynamics, in order to be able to consistently compare with the theoretical dihadron cross section in Sec. 2.1, we need to include gluon dijet channels from PGF and gluon-initiated resolved process in the comparison. However, as the measured observable in the real experiment is a mixture of different process, as illustrated in Eq. (2.7), we have to know how significant the signal from gluon saturation manifests itself in a mixed event sample. From the saturation-based predictions, a sizeable suppression of the away-side peak from $e + p$ to e+A is expected.

In the meanwhile, it is crucial to point out that parton showers suppress the away-side peak of the dihadron correlation function just like saturation does. However, currently it is still unclear how the parton shower effect is modified in the nuclear medium, without which it is hard to draw any definite conclusions about the saturation effects, as parton showers and saturation effects are always entangled. Nevertheless, thanks to the large kinematic coverage of eRHIC, one can explore the nuclear dependence of parton showers outside the saturation region by measuring dihadron correlations for different nuclei in the high Q^2 regime. This kinematic regime has a significant phase space for parton showers for this observable. More importantly, the measurement of dihadron correlations gives the opportunity to use the near-side peak of the correlation function as a reference to study the nuclear medium effects on parton showers as the saturation effects only manifest themselves in the away-side peak, as shown in Fig. 2.6.

In the saturation formalism, the parton shower contribution is effectively cast into the Sudakov factor for the DIS dijet process at small x. To illustrate this point, Fig. 2.8 shows the correlation function simulated with and without parton showers, compared to the corresponding theoretical predictions with and without Sudakov effects. The filled circles represent the PYTHIA simulation for $e + p$ without parton showers, and they agree very well with the solid line from the theoretical prediction including saturation effects, but excluding Sudakov effects. The comparison (empty circles and dashed line) between simulated PYTHIA $e + p$ data including parton showers and the theoretical predictions with saturation plus Sudakov effects is also good, especially considering the
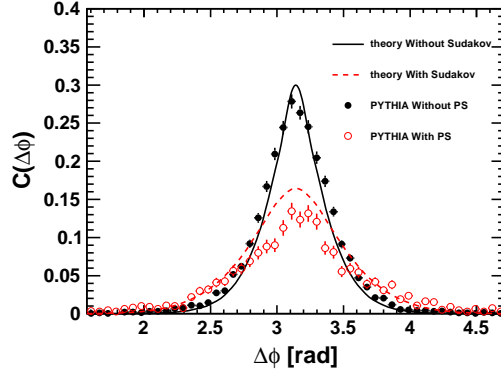
Figure 2.8: [color online] π^0 $\Delta\phi$ correlation comparing PYTHIA and theoretical saturation calculations for $e + p$ 10 GeV $\times$ 100 GeV for events from PGF and resolved gluon channel subprocesses at $1.0\,\mathrm{GeV}^2 < Q^2 < 2.0\,\mathrm{GeV}^2$, $0.65 < y < 0.75$, $p_T^{trig} > 2\,\mathrm{GeV}/c$, $1\,\mathrm{GeV}/c < p_T^{assoc} < p_T^{trig}$, $0.25 < z_h^{trig}, z_h^{assoc} < 0.35$. The solid and dashed curves show theoretical predictions including saturation effects for $e + p$ without and with Sudakov factor, respectively. The filled and empty circles illustrate PYTHIA simulations for $e + p$ without and with parton showers.

model uncertainties. Thus, the agreement in $e + p$ collisions enables one to estimate the nuclear medium effects on parton showers in the theoretical predictions for saturation including Sudakov effects.

Since the saturation effect decouples from hadronization, it does not depend on which specific particle type being detected. Although the theoretical prediction is made for π^0, the suppression factor from $e + p$ to e+A still holds for other different final state particles. In the next section, the significance for the suppression of gluon saturation will be shown for the charged hadrons $C(\Delta\phi)$ observable with limited statistics and expected background estimation.

2.2.3 Monte Carlo Results and Uncertainties

In order to guarantee the validity of perturbative calculations and avoid the kinematic regime of quasi-real photo-production, a cut of $Q^2 > 1\,\mathrm{GeV}^2$ is generally made. On the other hand, probing the saturation dynamics requires to probe the dense region,
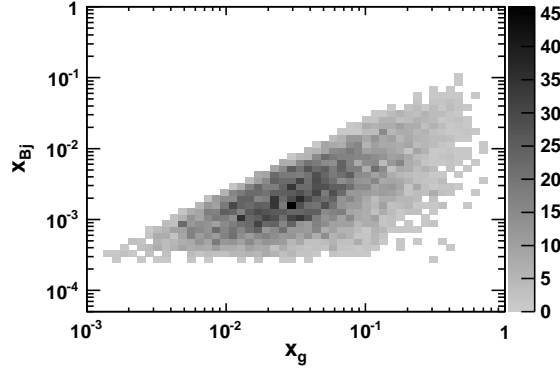
Figure 2.9: The correlation of x_{Bj} vs x_g for the PGF process for $e + p$ at 10 GeV × 100 GeV with $0.01 < y < 0.95$, $1\,\text{GeV}^2 < Q^2 < 20\,\text{GeV}^2$. A relatively broad correlation between these two variables is observed.

which means that one needs to go to low x and low-to-moderate Q^2 in the pursuit of saturation effects at a certain center of mass energy. A cut in transverse momentum of the charged hadron pairs is usually performed to pick particles from hard interactions. A cut on z_h is also imposed to reject particles from the target remnants. Thus, a typical cut to select dihadron pairs from hard parton scatterings is: $p_T^{trig} > 2$ GeV/c, $1\,\text{GeV}/c < p_T^{assoc} < p_T^{trig}, 0.2 < z_h^{trig}, z_h^{assoc} < 0.4$. To further explore the transition behavior in and out of the saturation region, we use three Q^2 bins: $1\,\text{GeV}^2 < Q^2 < 2\,\text{GeV}^2$, $3\,\text{GeV}^2 < Q^2 < 5\,\text{GeV}^2$ and $9\,\text{GeV}^2 < Q^2 < 20\,\text{GeV}^2$; and two y bins: $0.25 < y < 0.35$ and $0.6 < y < 0.8$. To study saturation physics using varying heavy ion beams, we focus on the $1\,\text{GeV}^2 < Q^2 < 2\,\text{GeV}^2$, $0.6 < y < 0.8$ bin, while the $9\,\text{GeV}^2 < Q^2 < 20\,\text{GeV}^2$ or $0.25 < y < 0.35$ bins serve as a reference for the behaviour without saturation effects. To pin down the nuclear dependence of parton showers, we compare the correlation between $e + p$ and e+A collisions for bins without saturation effects. Because the saturation scale Q_s varies with the gluon momentum fraction x_g, it is important to have access to x_g. Fig. 2.9 shows how, by utilizing x_{Bj}, one can effectively constrain the underlying x_g distribution. Although this is only a broad correlation, it is demonstrated in Fig. 2.10 that the typical x_g at a given x_{Bj} is constrained to a certain magnitude and can be used to separate the saturation region from the non-saturated region. Fig. 2.11 shows the
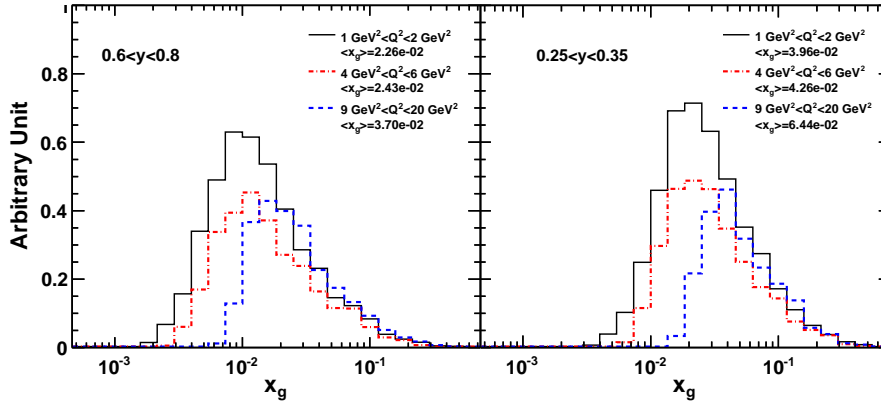
Figure 2.10: [color online] x_g distributions in various kinematics bins probed by the correlated hadron pairs in the PGF process for $e + p$ 10 GeV × 100 GeV.

η distribution of the trigger particle and the correlated particle in the aforementioned kinematic bins at 10 GeV × 100 GeV and 20 GeV × 100 GeV. Clearly, with a charged particle acceptance spanning $-4.5 < \eta < 4.5$, both trigger and associate particles in our kinematics binning scheme can be fully accepted by the detector.

As shown in Fig. 2.1, if we are in a kinematic regime in x and Q^2 where saturation effects are to be expected, the dihadron correlation function should exhibit a noticeable suppression of the away-side peak. The most promising kinematics bin to study this saturation signature at an EIC is $1 \, \text{GeV}^2 < Q^2 < 2 \, \text{GeV}^2$ and $0.6 < y < 0.8$.

In Fig. 2.12 we compare the strength of the coincidence probability based on a theoretical saturation model prediction for the away-side for $e + p$ and e+Au. The filled circles in Fig. 2.12 are simulated with PYTHIA for $e + p$ collisions, including detector smearing and acceptance effects. The projected e+Au saturated correlation function (open circles) is obtained by multiplying the $e + p$ histogram with the suppression factor $w_i^s = C(\Delta\phi)_{eAu}/C(\Delta\phi)_{ep}$ including Sudakov effects extracted from Fig. 2.1. This suppression factor can only be applied to dijet channels involving gluons; namely PGF and resolved $qg \to qg$, $gg \to gg$, $gg \to q\bar{q}$ subprocesses. The other quark initiated subprocesses have been simulated with PYTHIA using the non-saturated e+A model including nuclear PDFs and final-state energy loss. The uncertainties represent the statistical
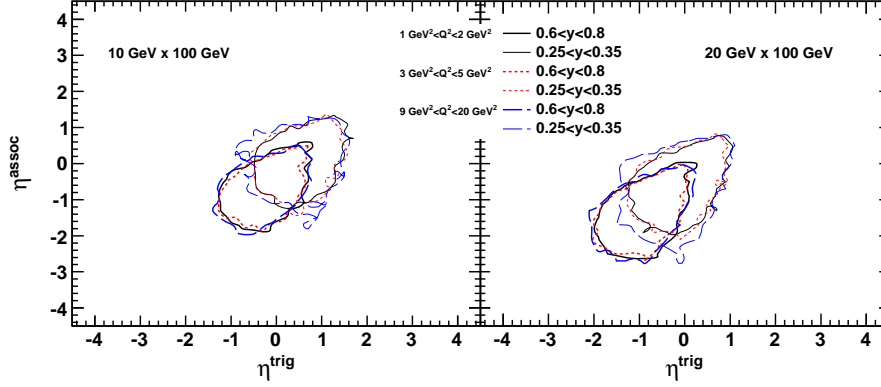
Figure 2.11: [color online] The contours show the η regions covered by the correlated dihadron pairs: for 10 GeV × 100 GeV and 20 GeV × 100 GeV. Thick lines mark out the region for $0.6 < y < 0.8$ while thin lines for $0.25 < y < 0.35$.

precision from an integrated luminosity of $1\,fb^{-1}$. The solid (dashed) lines in Fig. 2.12 represent fits to the simulated data points with (without) detector effects included in the simulation.

Since to date there is no exact knowledge of the saturation scale, the uncertainty in the suppression factor is estimated by varying the saturation scale by a factor of 0.5 and 2. The resulting uncertainty bands are depicted in Fig. 2.12. The suppression of the away-side peak remains significant even with this additional uncertainty compared to the e+Au curve shown in Fig. 2.7 accounting for nuclear effects in the parton distribution functions, energy loss effects and the resonance decay. In summary, the suppression effects on dihadron correlations due to saturation can be clearly discriminated from effects based on classical nuclear medium modifications with a well-designed EIC machine.
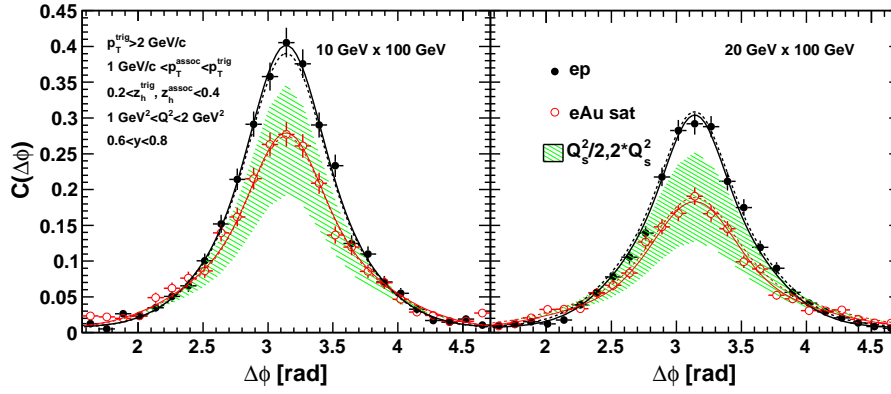
Figure 2.12: [color online] The correlation function at $1\,\mathrm{GeV}^2 < Q^2 < 2\,\mathrm{GeV}^2$, $0.6 < y < 0.8$ for an integrated luminosity of $1\,fb^{-1}$. The $e+p$ result comes from PYTHIA simulations. The $e+$Au results are a combination of simulations from a saturation-based model plus modified PYTHIA simulations. The suppression factor uncertainty was estimated by varying Q_s^2 by a factor of 0.5 and 2. Sudakov resummation has also been incorporated for $e+$Au. The solid lines represent a fit for the simulated pseudo-data including detector effects; the dashed line excludes detector effects.

References

[BSY78]   T. Bauer, R. Spital, D. Yennie, and F. Pipkin. The Hadronic Properties of the Photon in High-Energy Interactions, Rev.Mod.Phys. **50**, 261 1978.

[DJL11]   A. Dumitru, J. Jalilian-Marian, T. Lappi, B. Schenke, and R. Venugopalan. Renormalization group evolution of multi-gluon correlators in high energy QCD, Phys.Lett. **B706**, 219–224 2011, 1108.4764.

[DMM11]   F. Dominguez, A. Mueller, S. Munier, and B.-W. Xiao. On the small-x evolution of the color quadrupole and the Weizsácker-Williams gluon distribution, Phys.Lett. **B705**, 106–111 2011, 1108.1752.

[DMX11]   F. Dominguez, C. Marquet, B.-W. Xiao, and F. Yuan. Universality of Un-integrated Gluon Distributions at small x, Phys.Rev. **D83**, 105005 2011, 1101.0715.

[DQX12]   F. Dominguez, J.-W. Qiu, B.-W. Xiao, and F. Yuan. On the linearly polarized gluon distributions in the color dipole model, Phys.Rev. **D85**, 045003 2012, 1109.6293.

[EPS09]   K. Eskola, H. Paukkunen, and C. Salgado. EPS09: A New Generation of NLO and LO Nuclear Parton Distribution Functions, JHEP. **0904**, 065 2009, 0902.4154.

[FS00]   C. Friberg and T. Sjostrand. Total cross-sections and event properties from real to virtual photons, JHEP. **0009**, 010 2000, hep-ph/0007314.

[FSS07]   D. de Florian, R. Sassot, and M. Stratmann. Global analysis of fragmentation functions for pions and kaons and their uncertainties, Phys.Rev. **D75**, 114010 2007, hep-ph/0703242.

[GW98]   K. J. Golec-Biernat and M. Wusthoff. Saturation effects in deep inelastic scattering at low Q**2 and its implications on diffraction, Phys.Rev. **D59**, 014017 1998, hep-ph/9807513.

[MV94]   L. D. McLerran and R. Venugopalan. Computing quark and gluon distribution functions for very large nuclei, Phys.Rev. **D49**, 2233–2241 1994, hep-ph/9309289.

[MXY09]   C. Marquet, B.-W. Xiao, and F. Yuan. Semi-inclusive Deep Inelastic Scattering at small x, Phys.Lett. **B682**, 207–211 2009, 0906.1454.

[MXY13a]   A. Mueller, B.-W. Xiao, and F. Yuan. Sudakov Double Logarithms Resummation in Hard Processes in Small-x Saturation Formalism, Phys.Rev. **D88**, 114010 2013, 1308.2993.

[MXY13b]   A. Mueller, B.-W. Xiao, and F. Yuan. Sudakov Resummation in Small-x Saturation Formalism, Phys.Rev.Lett. **110**, 082301 2013, 1210.5792.

[MZ11]   A. Metz and J. Zhou. Distribution of linearly polarized gluons inside a large
          nucleus, Phys.Rev. **D84**, 051503 2011, 1105.1991.

[PSH02]   J. Pumplin *et al.* New generation of parton distributions with uncertainties
          from global QCD analysis, JHEP. **0207**, 012 2002, hep-ph/0201195.

[SW03]   C. A. Salgado and U. A. Wiedemann. Calculating quenching weights,
          Phys.Rev. **D68**, 014008 2003, hep-ph/0302184.

[WBG05]   M. Whalley, D. Bourilkov, and R. Group. The Les Houches accord PDFs
          (LHAPDF) and LHAGLUE, 2005, hep-ph/0508110.